

Fast and memory-efficient reconstruction of sparse Poisson data in listmode with non-smooth priors with application to time-of-flight PET

Georg Schramm¹ and Martin Holler²

¹Department of Imaging and Pathology, Division of Nuclear Medicine, KU Leuven, Belgium

²Institute of Mathematics and Scientific Computing, University of Graz, Austria. MH is a member of NAWI Graz (<https://www.nawigraz.at>) and BioTechMed Graz (<https://biotechmedgraz.at>).

Abstract

Objective: Complete time of flight (TOF) sinograms of state-of-the-art TOF PET scanners have a large memory footprint. Currently, they contain $\sim 4 \cdot 10^9$ data bins which amount to ~ 17 GB in 32 bit floating point precision. Moreover, their size will continue to increase with advances in the achievable detector TOF resolution and increases in the axial field of view. Using iterative algorithms to reconstruct such enormous TOF sinograms becomes increasingly challenging due to the memory requirements and the computation time needed to evaluate the forward model for every data bin. This is especially true for more advanced optimization algorithms such as the stochastic primal-dual hybrid gradient (SPDHG) algorithm which allows for the use of non-smooth priors for regularization using subsets with guaranteed convergence. SPDHG requires the storage of additional sinograms in memory, which severely limits its application to data sets from state-of-the-art TOF PET systems using conventional computing hardware.

Approach: Motivated by the generally sparse nature of the TOF sinograms, we propose and analyze a new listmode (LM) extension of the SPDHG algorithm for image reconstruction of sparse data following a Poisson distribution. The new algorithm is evaluated based on realistic 2D and 3D simulations, and a real dataset acquired on a state-of-the-art TOF PET/CT system. The performance of the newly proposed LM SPDHG algorithm is compared against the conventional sinogram SPDHG and the listmode EM-TV algorithm.

Main results: We show that the speed of convergence of the proposed LM-SPDHG is equivalent to the original SPDHG operating on binned data (TOF sinograms). However, we find that for a TOF PET system with 400 ps TOF resolution and 25 cm axial FOV, the proposed LM-SPDHG reduces the required memory from approximately 56 GB to 0.7 GB for a short dynamic frame with 10^7 prompt coincidences and to 12.4 GB for a long static acquisition with $5 \cdot 10^8$ prompt coincidences.

Significance: In contrast to SPDHG, the reduced memory requirements of LM-SPDHG enables a pure GPU implementation on state-of-the-art GPUs - avoiding memory transfers between host and GPU - which will substantially accelerate reconstruction times. This in turn will allow the application of LM-SPDHG in routine clinical practice where short reconstruction times are crucial.

1 Introduction

A major challenge of image reconstruction in positron emission tomography (PET) is noise suppression since the acquired emission data suffer from high levels of Poisson noise due to limitations in acquisition time, injectable dose and scanner sensitivity. To limit the transfer of the data noise into the image during model-based iterative reconstruction (MBIR), different strategies exist. One possibility is to add a “smoothing” prior to the data fidelity term in the cost function that is being optimized. In general, we can formulate the resulting optimization problem for any imaging system where the acquired data follow a Poisson distribution as

$$\operatorname{argmin}_{x \geq 0} \sum_{i=1}^m \underbrace{(Px + s)_i - d_i \log((Px + s)_i)}_{D_i((Px+s)_i)} + \beta R(Kx), \quad (1)$$

where x is the image to be reconstructed, P is the linear forward model, d are the acquired data and s are additive contaminations. $\sum_{i=1}^m D_i((Px + s)_i)$ is the negative Poisson log-likelihood, i is the index of the data bin and m is the total number of data bins. In the specific case of time of flight (TOF) PET, P is the time of flight (TOF) PET forward model including the effects of attenuation, normalization and limited

spatial resolution, d are the acquired prompt TOF PET coincidences (the emission sinogram), and s are the estimated random and scattered coincidences.

$R(K\cdot)$ is a ‘‘smoothing prior’’ consisting of a generic linear operator K that calculates local differences and a proper, convex, lower-semicontinuous function R . The level of regularization is controlled by the non-negative scalar factor β . A specific example for K would be the gradient operator ∇ , e.g. approximated by finite forward differences in the discretized setting. Combining the gradient operator for K with the mixed L2-L1 norm for R leads to the well-known Total Variation (TV) prior [1].

The TV prior, as well as many other advanced smoothing priors aiming for edge-preservation such as e.g. Total Generalized Variation (TGV) [2], Joint T(G)V [3, 4] Parallel Level Sets [5, 6] or directional Total Variation (DTV) [7], require the use of non-smooth functions for R as instrumental building block. This prevents the use of simple and efficient purely gradient-based optimization algorithms to solve (1).

PDHG and SPDHG for PET reconstruction with non-smooth priors

Using the fact that $z \mapsto D(z) := \sum_{i=1}^m D_i(z_i)$ and $z \mapsto \beta R(z)$ are convex, lower-semicontinuous functions and thus are equal to their convex biconjugates $D^{**}(z) = \sup_y \langle z, y \rangle - \sum_{i=1}^m D_i^*(y_i)$ and $(\beta R)^{**}(z) = \sup_w \langle z, w \rangle - (\beta R)^*(w)$, respectively, where D_i^* and $(\beta R)^*$ are the convex conjugates, and that $(\beta R)^*(w) = \beta R^*(w/\beta)$, we can rewrite (1) as the saddle point problem

$$\operatorname{argmin}_{x \geq 0} \sup_{y, w} \langle Px + s, y \rangle + \langle Kx, w \rangle - \sum_{i=1}^m D_i^*(y_i) - \beta R^*(w/\beta), \quad (2)$$

introducing the dual variables y and w , and the convex dual of the Poisson log-likelihood given as

$$D_i^*(y_i) = \begin{cases} -d_i + d_i \log\left(\frac{d_i}{1-y_i}\right) & \text{if } y_i < 1 \text{ and } d_i > 0, \\ 0 & \text{if } y_i \leq 1 \text{ and } d_i = 0, \\ \infty & \text{else.} \end{cases} \quad (3)$$

Under mild assumptions on R , which hold for all of the above-mentioned smoothing priors, Problem (2) is equivalent to (1) and can be solved even for non-smooth priors using the generic primal-dual hybrid gradient (PDHG) algorithm by Chambolle and Pock [8]. PDHG is an iterative algorithm that requires the evaluation of the complete forward and adjoint operator in every update. The usage of the original PDHG algorithm to solve (2) for real-world state-of-the-art TOF PET systems, however, usually results in extremely long computation times, because the evaluation of P and P^T for state-of-the-art TOF PET systems is computationally very demanding, and because several hundreds to thousands of updates are needed to obtain reasonable convergence.

To overcome this limitation, Chambolle et al. published a stochastic extension of PDHG called SPDHG for saddle point problems that are separable in the dual variable in 2018 [9]. In contrast to PDHG, SPDHG has the advantage that the complete forward and adjoint operator are split into n subsets, and that, in every update, only a random subset of the forward and adjoint operator chosen according to a probability p_k has to be evaluated. In [10], Ehrhardt et al. applied SPDHG to 3D non-TOF PET reconstruction with TV-like priors and showed that around 10 complete projections and back projections can be sufficient to obtain reasonable convergence using SPDHG with 252 subsets. Moreover, the authors also demonstrated that preconditioning further accelerates convergence. The resulting SPDHG algorithm to solve (2) is summarized in Algorithm 1, where the proximal operator for a convex function f using the weighted norm $\|\cdot\|_M^2 = \langle M^{-1}\cdot, \cdot \rangle$ induced by a symmetric and positive-definite matrix M is defined as

$$\operatorname{prox}_f^M(y) = \operatorname{argmin}_v \left(\frac{1}{2} \|v - y\|_M^2 + f(v) \right). \quad (4)$$

For the convex conjugate of the negative Poisson log-likelihood D_i^* , this proximal operator can be calculated point-wise and is given by

$$\begin{aligned} (\operatorname{prox}_{D_i^*}^{S_i}(y))_i &= \operatorname{prox}_{D_i^*}^{S_i}(y_i) \\ &= \frac{1}{2} \left(y_i + 1 - \sqrt{(y_i - 1)^2 + 4S_i d_i} \right). \end{aligned} \quad (5)$$

Algorithm 1 SPDHG for PET reconstruction [10]

```
1: Initialize  $x(=0), y(=0), (w=0), (S_i)_i, T, (p_i)_i$ 
2:  $\bar{z} = z = P^T y + K^T w$ 
3: repeat
4:    $x \leftarrow \text{proj}_{\geq 0}(x - T\bar{z})$ 
5:   Select  $i \in \{1, \dots, n+1\}$  randomly according to  $(p_i)_i$ 
6:   if  $i \leq n$  then
7:      $y_i^+ \leftarrow \text{prox}_{D_i^{S_i}}(y_i + S_i(P_i x + s_i))$ 
8:      $\delta z \leftarrow P_i^T(y_i^+ - y_i)$ 
9:      $y_i \leftarrow y_i^+$ 
10:  else
11:     $w^+ \leftarrow \beta \text{prox}_{R^*}^{S_i/\beta}((w + S_i K x)/\beta)$ 
12:     $\delta z \leftarrow K^T(w^+ - w)$ 
13:     $w \leftarrow w^+$ 
14:  end if
15:   $z \leftarrow z + \delta z$ 
16:   $\bar{z} \leftarrow z + (\delta z/p_i)$ 
17: until stopping criterion fulfilled
18: return  $x$ 
```

The proximal operator for R^* obviously depends on the choice of R but can be also efficiently computed using point-wise operations for many popular choices of R . As mentioned in [10], Algorithm 1 converges if we use the preconditioned step sizes

$$S_k = \gamma \text{diag}\left(\frac{\rho}{P_k \mathbf{1}}\right) \quad T_k = \gamma^{-1} \text{diag}\left(\frac{\rho p_k}{P_k^T \mathbf{1}}\right),$$

and

$$S_{n+1} = \gamma \frac{\rho}{\|K\|} \quad T_{n+1} = \gamma^{-1} \frac{p_{n+1} \rho}{\|K\|},$$

setting $T = \min_{k=1, \dots, n+1} T_k$ pointwise, and choosing $0 < \rho < 1$ and $\gamma > 0$.

Limitations of PDHG and SPDHG for PET reconstruction

Whilst SPDHG is a big step forward for an efficient solution of (2) in terms of computational speed, SPDHG also comes with two main limitations. First, as discussed in Remark 2 of [10], a potential drawback of SPDHG is that it requires keeping at least one more complete (TOF) sinogram in memory (the dual variable y). Moreover, if the proposed preconditioning is used, a second complete (TOF) sinogram (the sequence of step sizes $(S_k)_{k=1}^n$) needs to be stored in memory. Storing one or two extra sinograms in memory of modern computers is not a major problem for static single-bed non-TOF PET data, where sinogram sizes are relatively small. However, for simultaneous multi-bed, dynamic or TOF PET data, the size of the complete data sinograms can become problematic. This issue gets even more severe when aiming for a complete GPU implementation of Algorithm 1 since the available memory on state-of-the-art GPUs is nowadays much smaller compared to CPUs.

As an example, for a TOF PET scanner with 25 cm axial FOV and a TOF resolution of ca. 400 ps, a complete unmashed static TOF sinogram for one bed position has approximately $4.4 \cdot 10^9$ data bins, requiring ca. 17 GB of memory in 32 bit floating point precision. Note that with improved TOF resolution and increasing axial field of view (e.g. total body PET scanners), the memory required to store a complete TOF sinogram will continue to substantially increase in the future.

Second, PDHG and SPDHG only work with “binned” data. In the case of TOF PET reconstruction, that means that the acquired raw listmode data first need to be binned into TOF sinograms and that P and P^T need to be evaluated using sinogram projectors. For most acquisitions with modern TOF PET scanners, this is inefficient both in terms of memory and computational time since the TOF emission data are extremely sparse. In contrast, storage and processing of the data in listmode format (event by event) is usually more efficient.

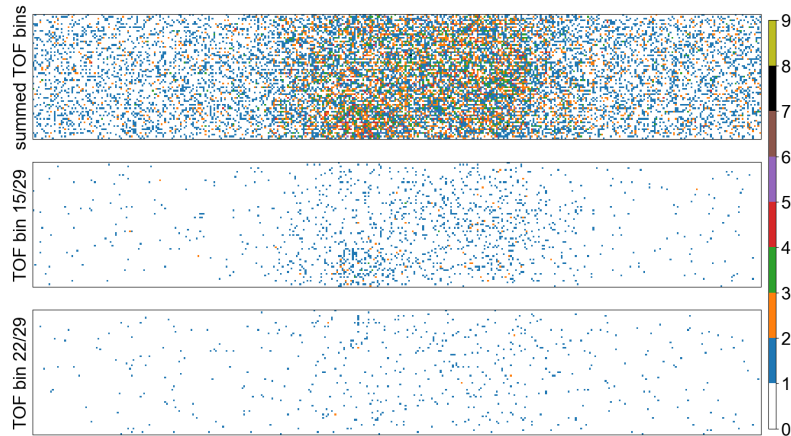


Figure 1: Representative slices through a single view of an emission sinogram of a 80s ^{18}F FDG acquisition of a liver bed position. The scan was acquired 1 h post injection with an injected dose of 323 MBq on a GE DMI PET/CT with a TOF resolution of 400 ps (29 TOF bins). The horizontal and vertical axis represent the radial and axial direction (direct planes only), respectively. (top) sum over all TOF bins. (middle) central TOF bin 15/29 with 94% empty bins. (bottom) TOF bin 22/29 with 97% empty bins.

Sparsity of TOF PET data

Compared to non-TOF PET emission sinograms, TOF PET emission sinograms of most acquisitions with state-of-the-art TOF PET scanners are extremely sparse. This is because every geometrical line of response (LOR) has to be subdivided into several small TOF bins. To achieve sufficient sampling of the TOF information, the number of TOF bins has to be inversely proportional to the TOF resolution of the scanner. Consequently, for a fixed number of acquired prompt coincidences, the sparsity of the sinogram is proportional to the TOF resolution.

As an example, for a typical 80 s acquisition of a liver bed position in an FDG scan with an injected dose of 323 MBq acquired 60 min p.i. on a state-of-the-art TOF PET/CT scanner with 20 cm axial FOV, more than 94% of the data (TOF sinogram) bins are empty. An example that demonstrates this extreme sparsity of TOF sinograms is shown in Fig. 1. For shorter frames, as present, e.g., in the early phase of dynamic scans or when respiratory or cardiac gating is used, the fraction of empty bins can even higher.

Note that we expect that the sparsity of the TOF PET emission data of future PET systems will increase faster than linear compared to the improvement of the TOF resolution. This is because with better TOF resolution, every detected event carries more information such that fewer detected events are needed to reconstruct images with the similar variance [11]. Moreover, the method presented in this work is applicable not only to TOF PET image reconstruction, but to all imaging reconstruction problems with sparse data following a Poisson distribution such as (low count) SPECT or photon counting CT.

Contributions and Aim

To improve the efficiency of SPDHG in terms of required memory and computation time when reconstructing sparse TOF PET data, we propose and analyze a listmode extension of the SPDHG algorithm called LM-SPDHG that allows event-by-event processing using dedicated listmode forward and back projectors. We first derive LM-SPDHG from SPDHG and show that the convergence of LM-SPDHG is as fast as the convergence of SPDHG based on dedicated numeric examples in 2D. Moreover, we analyze the memory requirements for LM-SPDHG compared to SPDHG for typical scans acquired on state-of-the-art TOF PET scanners.

We emphasize that the focus of this work is not on finding the optimal (non-smooth) prior or prior strength for a given clinical task in PET imaging. Instead, we aim to provide a framework enabling fast and memory efficient reconstruction of sparse TOF PET listmode data which will finally facilitate future research on the use of (non-smooth) priors in PET reconstruction.

2 Theory and Algorithms

Before deriving LM-SPDHG, the next subsection first of all shows how to reduce the memory requirements of SPDHG when reconstructing sparse TOF sinograms.

Memory-efficient SPDHG for sparse TOF sinograms

As shown in [12], the memory requirements for SPDHG can be substantially reduced by choosing a better initialization of the dual variable y .

From Eq. (5) we can observe that for data bins i where $d_i = 0$ (bins in the TOF emission sinogram with zero counts), $\text{prox}_{D_i^*}(a_i) = 1$ for $a_i \geq 1$ and $\text{prox}_{D_i^*}(a_i) = a_i$ otherwise. Moreover, provided that $y_i \geq 1$, we see that $a_i = y_i + S_i(P_i x + s_i) \geq 1$ since all other quantities are non-negative. Consequently, if we initialize all bins of y where the data sinogram d equals zero with one, these bins of y remain 1 during all iterations. This in turn means that these bins do not contribute to the update of δz , z , \bar{z} , and x , since only the difference between y and y^+ is backprojected in line 8 of Algorithm 1 meaning that all bins without data do not have to be kept in memory during the iteration loop (lines 3 until 17). The only place where the empty data bins contribute is the initialization of z and \bar{z} in line 2. However, this single back projection can be split into smaller chunks to also reduce the required memory of this step.

While at a first glance, the initialization of y proposed above might seem artificial, in fact it directly corresponds to choosing the optimal value for those y_i where $d_i = 0$. To see this, note that an optimal solution $(\hat{x}, \hat{y}, \hat{w})$ of (2) in particular needs to satisfy the optimality condition

$$P\hat{x} \in \partial D^*(\hat{y}), \quad (6)$$

where ∂D^* is the subdifferential of D^* . Since this is equivalent to $\hat{y} \in \partial D(P\hat{x})$, and since D (the negative Poisson log likelihood) is differentiable this leads to the condition

$$\hat{y} = 1 - \frac{d}{P\hat{x} + s}, \quad (7)$$

where the division is to be understood point-wise. With this we see that the proposed initialization directly corresponds to choosing the optimal value for y_i where $d_i = 0$, which is known explicitly in this case.

As argued above, this improved initialization of y naturally reduces the memory requirements of SPDHG and also improves the speed of convergence when a “warm start” for x^0 is chosen. The latter can, e.g., be achieved by applying one iteration and a reasonable amount of subsets of the EM-TV algorithm [13, 14]. Since in EM-TV every update is split into a classical EM step followed by a weighted denoising optimization problem in image space, EM-TV can be used in listmode as well by simply modifying the EM step.

Listmode SPDHG

As indicated by the name, emission data in listmode format are a chronological list N of detected events $e \in N$, where each event is characterized by a small set of (integer) numbers (e.g. the number of the two detectors, the discretized TOF difference, and a time stamp). To process the listmode data during reconstruction without binning it into a sinogram, we introduce the listmode forward operator P_N^{LM} mapping the image data x to a data-vector of dimension $|N|$ via

$$(P_N^{LM} x)_e = (Px)_{i_e}, \text{ for each } e \in N, \quad (8)$$

where i_e is the sinogram bin in which event e was detected. Also, we denote by s^{LM} with $s_e^{LM} = s_{i_e}$ the listmode-based scatter and random estimate.

Re-writing the gradient of the negative Poisson log likelihood using listmode data and the listmode operators is straightforward, such that any gradient-based PET reconstruction algorithm can be easily adapted to listmode data.

For a Bayesian approach with prior $R(K \cdot)$ as in (1) this is less immediate, but we can show that indeed (1) can be equivalently re-written into a minimization problem involving only the listmode forward operator

Algorithm 2 LM-SPDHG for PET reconstruction

```
1: Input event list  $N$ , contamination list  $s_N$ 
2: Calculate event counts  $\mu_e$  for each  $e$  in  $N$  (see text)
3: Initialize  $x, w, (S_i)_i, T, (p_i)_i$ 
4: Initialize list  $y_N = 1 - (\mu_N / (P_N^{LM} x + s_N))$ 
5: Preprocessing  $\bar{z} = z = P^T \mathbf{1} - P^{LM^T} (y_N - 1) / \mu_N + K^T w$ 
6: Split lists  $N, s_N$  and  $y_N$  into  $n$  sublists  $N_i, y_{N_i}$  and  $s_{N_i}$ 
7: repeat
8:    $x \leftarrow \text{proj}_{\geq 0}(x - T\bar{z})$ 
9:   Select  $i \in \{1, \dots, n+1\}$  randomly according to  $(p_i)_i$ 
10:  if  $i \leq n$  then
11:     $y_{N_i}^+ \leftarrow \text{prox}_{D^*}^{S_i} (y_{N_i} + S_i (P_{N_i}^{LM} x + s_{N_i}^{LM}))$ 
12:     $\delta z \leftarrow P_{N_i}^{LM^T} \begin{pmatrix} y_{N_i}^+ - y_{N_i} \\ \mu_{N_i} \end{pmatrix}$ 
13:     $y_{N_i} \leftarrow y_{N_i}^+$ 
14:  else
15:     $w^+ \leftarrow \beta \text{prox}_{R^*}^{S_i/\beta} ((w + S_i K x) / \beta)$ 
16:     $\delta z \leftarrow K^T (w^+ - w)$ 
17:     $w \leftarrow w^+$ 
18:  end if
19:   $z \leftarrow z + \delta z$ 
20:   $\bar{z} \leftarrow \bar{z} + (\delta z / p_i)$ 
21: until stopping criterion fulfilled
22: return  $x$ 
```

that is of the same form as (1) as shown in appendix A. This allows us to extend the SPDHG algorithm for listmode data and yields the algorithm as shown in Algorithm 2.

In contrast to the original SPDHG using binned data (sinograms), the forward and adjoint PET operators (lines 11 and 12) have been replaced by their listmode equivalents as in (8). Moreover, the dual variable for the data fidelity is replaced by the list y_N , which has the same length as the measured event list N . If an event with a fixed sinogram bin i_e occurs more than once in the event list N , it is also forward and back-projected multiple times in steps 11 and 12. To compensate for this fact, the algorithm divides by the event count¹ μ_e before back projection in line 12. Note that (i) as shown in Fig. 1 in most standard acquisitions the event count of most events is 1 and that (ii) calculating the event count μ_e which is a prerequisite creates a small pre-processing overhead (step 2). However, when implemented on a modern GPU this overhead is small compared to the computation time needed to calculate all iterations. Moreover, it is in the similar order of the time needed to unlist the native listmode data into a sinogram which is a prerequisite and pre-processing overhead for SPDHG.

Another difference of LM-SPDHG compared to SPDHG is the fact that we split the data into n subsets by assigning every n -th event of the complete event list N to the n -th sub list - as commonly done when defining subsets in listmode OSEM. In that way, we can think of the subset listmode forward operator $P_{N_i}^{LM}$ as the full forward operator P with a sensitivity reduced by a factor of n . Accordingly, we set the step sizes associated with the subset listmode PET operators to

$$S_k = \gamma \text{diag}\left(\frac{\rho}{P_{N_k}^{LM} \mathbf{1}}\right) \quad T_k = \gamma^{-1} \text{diag}\left(\frac{\rho p_k}{P^T \mathbf{1} / n}\right). \quad (9)$$

At a first glance, the initialization of z and \bar{z} in step 5 of Algorithm 2 might look odd. However, the first part of the expression is equivalent to applying the adjoint sinogram operator P^T to a sinogram initialized according to (7). Note that step 5 still requires to calculate a sinogram back projection of a unity sinogram ($P^T \mathbf{1}$) which we would like to avoid in listmode data processing. Unfortunately, avoiding this single sinogram backprojection is not possible. However, note that this “sensitivity image“ is also needed in

¹the event count μ_e represents the number of times the event e occurs in the event list N . For TOF PET, a data bin is characterized by the combination of geometrical LOR and the TOF bin along the LOR (a bin in a TOF sinogram).

		counts		
		5e8	7e7	1e7
	9 images	0.45 GB	0.45 GB	0.45 GB
SPDHG	1 uint, 3 float sino.	55.6 GB	55.6 GB	55.6 GB
LM-	9 images	0.45 GB	0.45 GB	0.45 GB
SPDHG	event list, 1 uint, 3 float lists	12.0 GB	1.7 GB	0.3 GB
	9 images	0.45 GB	0.45 GB	0.45 GB
EM-TV	event list, 2 float list	9.0 GB	1.3 GB	0.2 GB

Table 1: Estimation of required memory for SPDHG and LM-SPDHG assuming an image size of (300,300,125) and a TOF sinogram with 357 radial elements, 224 views, 1981 direct and oblique planes, and 27 TOF bins corresponding to a TOF PET scanner with 400 ps TOF resolution and 25 cm axial FOV for three counts levels. 5e8 counts approximately correspond to a high count 20 min late static FDG brain scan, 7e7 counts to an 80 s static FDG body bed position 1 h p.i., and 1e7 counts to a short early frame in a dynamic acquisition. In this estimation, we assume that every TOF PET listmode event can be encoded using 10 bytes.

the calculation of the step sizes T_k and also in the listmode EM-TV algorithm that we use to initialize x . Hence, we recommend pre-computing the sensitivity image ($P^T 1$) and storing it in memory.

In summary, compared to SPDHG, LM-SPDHG as shown in Algorithm 2 has the advantage that (i) only lists (N, y_N, s_N, μ_N) instead of complete sinograms (y and d) have to be stored in memory and (ii) all projections and back projections can be performed using listmode projectors. This means that for all acquisitions where the number of detected events is substantially smaller than the number of data bins, the required memory and computation time is reduced. The latter depends on the actual implementation of the sinogram and listmode projectors and on the computational hardware. According to our experience using a state-of-the-art GPU implementation of Joseph projectors [15] for a TOF PET scanner with 400 ps TOF resolution and 25 cm axial field of view, a forward and back projection is faster in listmode if approximately less than $3e8$ events have to be processed. For $7e7$ and $1e7$ counts, the projections are approximately faster by a factor of 3 and 5, respectively². Note that the difference in the computation time of the projection for sinogram and listmode depends on the specific implementation - especially on the optimization of the memory access - and the computational hardware. A detailed comparison of the required memory for SPDHG and LM-SPDHG for different typical PET acquisitions is listed in Table 1.

3 Numerical Experiments

Recalling the fact that for most common TOF PET acquisitions, LM-SPDHG requires less memory and is also faster, one would probably prefer LM-SPDHG over SPDHG if the speed of convergence is the same. In the following, we describe a set of numerical experiments that we conducted to show that this is indeed the case. In the absence of an analytical solution to the optimization problems (1) and (2), we analyzed the convergence of LM-SPDHG and SPDHG with respect to a reference solution x^* as done in [10]. Convergence was monitored by tracking the relative cost function

$$c_{\text{rel}}(x) = (c(x) - c(x^*)) / (c(x^0) - c(x^*)), \quad (10)$$

where $c(x)$ is the cost function to be optimized in (1) and x^0 is the initialization used for x . Moreover, convergence was also monitored in image space by tracking the peak signal-to-noise ratio with respect to x^*

$$\text{PSNR}(x) = 20 \log_{10} \left(\|x^*\|_{\infty} / \sqrt{\text{MSE}(x, x^*)} \right), \quad (11)$$

where MSE is the mean squared error. The reference solution was obtained by running the deterministic PDHG (SPDHG without subsets) for 20000 iterations. Since running PDHG with 20000 iterations using realistic 3D TOF PET data takes a very long time (approx. 250 h), all numerical convergence experiments were performed using simulated 2D TOF PET data. A 2D software brain phantom with a gray to white

²The reported computational times for the projections include the time needed to transfer the image and projection data to and from host to the GPU and thus correspond to a hybrid CPU/GPU computational model.

Algorithm 3 listmode EM-TV for PET reconstruction [13, 14]

- 1: **Input** event list N , contamination list s_N
 - 2: **Split** lists N and s_N into n sublists N_i , and s_{N_i}
 - 3: **Pre-compute** sensitivity image $g = P^T \mathbf{1}$
 - 4: **repeat**
 - 5: Select subset i
 - 6: $z \leftarrow \frac{x^n}{g} P_{N_i}^{LMT} \frac{1}{P_{N_i}^{LM} + s_{N_i}}$ (subset EM step)
 - 7: $w \leftarrow g/(\beta x)$
 - 8: $x^+ \leftarrow \operatorname{argmin}_{u \geq 0} \sum_j \frac{w_j}{2} (u_j - z_j)^2 + R(Ku)$
 - 9: **until** stopping criterion fulfilled
 - 10: **return** x
-

matter contrast of 4:1 was created based on the brainweb phantom [16] and used to generate simulated 2D TOF data including the effects of limited spatial resolution, attenuation and a flat contamination mimicking random and scattered coincidences with a contamination fraction of 42%. The geometry and TOF resolution of the simulated 2D PET system was chosen to mimic one direct plane of a state-of-the-art TOF PET scanner with a ring diameter of 650 mm and a 400 ps TOF resolution (sinogram dimension: 357 radial bins, 224 projection angles, 27 TOF bins). Noisy simulated prompt emission TOF sinograms and corresponding listmode data were generated for two different count levels (5e5 and 5e6 prompt counts). Unless stated otherwise, we always applied the EM-TV algorithm, summarized in Algorithm 3, using 1 iteration and 28 subsets to initialize x^0 and y^0 according to (7). To solve the weighted denoising problem in step 8 of the EM-TV algorithm, we applied the accelerated PDHG algorithm [8] using 20 iterations. In all SPDHG and LM-SPDHG reconstructions, the step size ratio γ was set to $3/\|x^0\|_\infty$ and ρ was set to 0.999. When splitting the data into n subsets, the vector of probabilities determining whether an update with respect to a subset of the data or with respect to the prior is done was set to

$$p_k = \begin{cases} \frac{1}{2n} & \text{if } k \leq n \\ \frac{1}{2} & \text{else,} \end{cases} \quad (12)$$

such that on average an update with respect to the prior was done on every second update as suggested in [10]. In this work, we use the term iteration for $2n$ updates such that on average in every iteration the complete data are forward and backprojected once and n updates with respect to the prior are performed. As benchmark examples for non-smooth priors, we consider two ‘‘Total Variation like’’ priors in this work. These priors have the form

$$R(Kx) = \|Kx\|_{2,1} = \sum_i \sqrt{\sum_j (Kx)_{ij}^2}, \quad (13)$$

where $\|Kx\|_{2,1}$ is the sum over all entries of the pointwise Euclidean norm of Kx (mixed L2-L1 norm). The proximal operator for the convex dual of this prior is given by

$$(\operatorname{prox}_{R^*}^S(w))_i = \frac{w_i}{\max(1, |w_i|)}. \quad (14)$$

For the linear operator K , we first used the finite forward difference operator resulting in the classical Total Variation (TV) prior [1]. Moreover, we also implemented the Directional Total Variation (DTV) prior incorporating structural information by only considering the component of the finite difference vector in every voxel that is perpendicular to the spatial gradient of a prior image in that voxel [7]. In our convergence experiments using DTV, we assumed perfect structural prior information meaning that the prior image used for DTV, was the image itself with a flipped contrast. Note that in real acquisitions the quality of the available structural prior information is of course inferior. However, we do not expect that this fact strongly affects the convergence properties of SPDHG and LM-SPDHG.

To demonstrate that LM-SPDHG also works for realistic 3D TOF PET listmode data, we simulated and reconstructed 3D TOF PET data based on the 3D XCAT [17] phantom and a state-of-the-art TOF PET

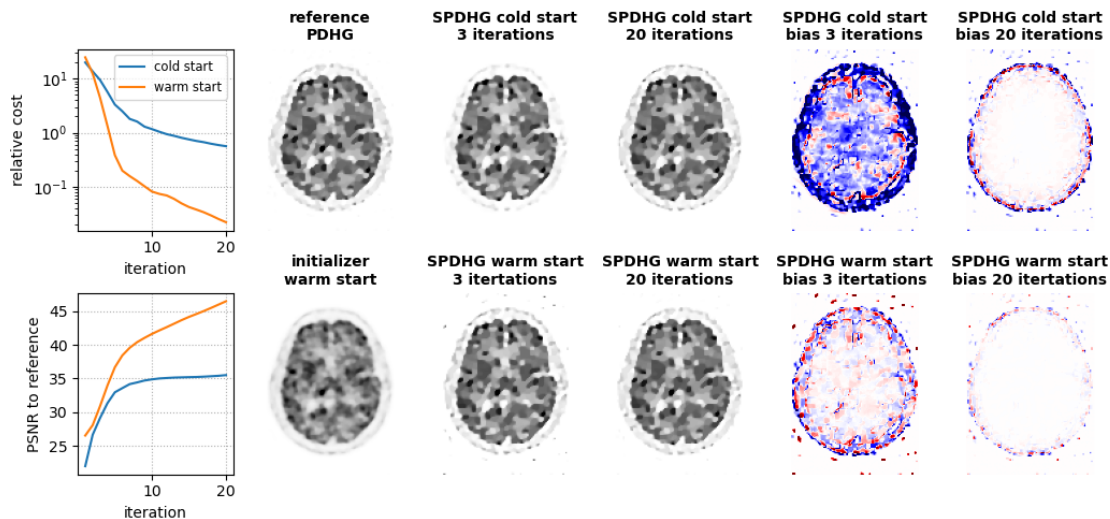


Figure 2: Comparison of convergence of sinogram SPDHG using a cold and warm start for $3e5$ counts and a TV prior with $\beta = 0.03$ using 224 subsets. For the warm start, x^0 was taken from 1 EM-TV iteration with 28 subsets and y^0 was calculated according to (7). Left column: relative cost and PSNR with respect to the reference solution as a function of the iterations. Second column: reference PDHG reconstruction using 20000 iterations (top) and initializer x^0 used in the warm start. Third column: Reconstructions after 3 iterations with cold start (top) and warm start (bottom). Fourth column: Reconstructions after 20 iterations. Fifth and sixth column: Absolute differences of the SPDHG reconstructions with respect to the reference PDHG reconstruction. The range of the color map for the difference images is $\pm 10\%$ of the maximum of the reference reconstruction. Note that in the calculation of the relative cost the same x^0 was used and that in both cases the same step size ratio γ was used. Moreover, in the very early iterations the relative cost of SPDHG is greater 1 meaning that the cost is worse compared the the initialization. This is due to the fact that (S)PDHG in general is a non-monotonic algorithm.

scanner with 20 cm axial field of view, a ring diameter of 650 mm and a 400 ps TOF resolution (sinogram dimension: 357 radial bins, 224 projection angles, 1296 direct and oblique planes, 27 TOF bins). As before, the data simulation included the effects of attenuation, finite resolution and a flat contamination with a contamination fraction of 42%. In total, $7e7$ prompt counts were simulated corresponding approximately to a standard 80 s 1 h p.i. FDG liver bed position acquisition. Simulated listmode data were reconstructed using LM-SPDHG with 50 iterations and 224 subsets.

Last but not least, we also reconstructed a real TOF PET data set of the NEMA image quality phantom acquired on a GE Discovery MI 4 ring TOF PET/CT [18] (20 cm axial FOV, sinogram dimension: 357 radial bins, 272 projection angles, 1261 direct and oblique planes, 29 TOF bins, 400 ps TOF resolution). The activity contrast between the sphere inserts and the background was 10:1 and the acquisition contained $4.7e7$ prompt ($2.2e7$ true) coincidences. Reconstructions using a TV prior with $\beta = 6$ were performed with EM-TV using 100 iterations with 1 and 28 subsets, and with LM-SPDHG using 100 iterations and 224 subsets. We also performed a reconstruction of the same data set with LM-PDHG using 20000 iterations and 1 subset. This reconstruction was used as a reference to calculate the relative cost and PSNR.

All reconstruction algorithms used in this work were implemented in python3 using the open-source “parallelproj” CUDA projector libraries available at <https://github.com/gschramm/parallelproj>. An Nvidia V100 GPU with 16 GB RAM was used to perform all reconstructions. Upon publication of this article, an open-source implementation of the LM-SPDHG algorithm will be made available in the associated “pyparallelproj” python package. Preprocessing of the NEMA image quality phantom data set was performed using GE’s duetto PET reconstruction toolbox v2.17.

SPDHG using a warm start vs a cold start

Before investigating the convergence behavior of LM-SPDHG, we first tested whether a warm start could already help to lead to faster convergence of SPDHG using sinograms. Figure 2 shows the results of SPDHG reconstructions with a cold ($x^0 = 0$ and $y^0 = 0$) and warm start as described above for a data

set with $3e5$ true counts and a TV prior with $\beta = 0.03$. It can be seen that SPDHG with the warm start performs better in terms of relative cost and PSNR with respect to the reference reconstruction. A similar trend was observed for higher count levels, with different β values and using the DTV prior indicating that as expected the warm start helps to accelerate convergence in the early iterations.

Convergence of LM-SPDHG compared to SPDHG

Figure 3 summarizes the convergence comparison between sinogram SPDHG and LM-SPDHG for the same data set and prior as described in the previous subsection using the same warm start for both algorithms. As demonstrated by the convergence metrics and the reconstructed images, the convergence of sinogram SPDHG and LM-SPDHG is almost identical. This also holds for different count levels and for the structural DTV priors as shown in subfigures (b) and (c) and for different levels of regularization as shown in supplementary Figs. 1 and 2. For the example with the DTV prior shown in subfigure (c), the convergence in terms of PSNR seems to be even slightly faster with LM-SPDHG, which can be also seen in the difference images with respect to the reference reconstruction.

Convergence of LM-SPDHG compared to listmode EM-TV

A comparison between the convergence of LM-SPDHG using 224 subsets and listmode EM-TV using 1, 7 and 28 subsets is shown in Fig. 4. In all sub figures, LM-SPDHG converges much faster than EM-TV. Interestingly, when using listmode EM-TV with more than one subset, the convergence metrics saturate meaning that the algorithm remains on a limited cycle and the optimal solution is not reached. When using one subset, the convergence of EM-TV is much slower but does not seem to saturate after 100 iterations.

Convergence vs number of subsets

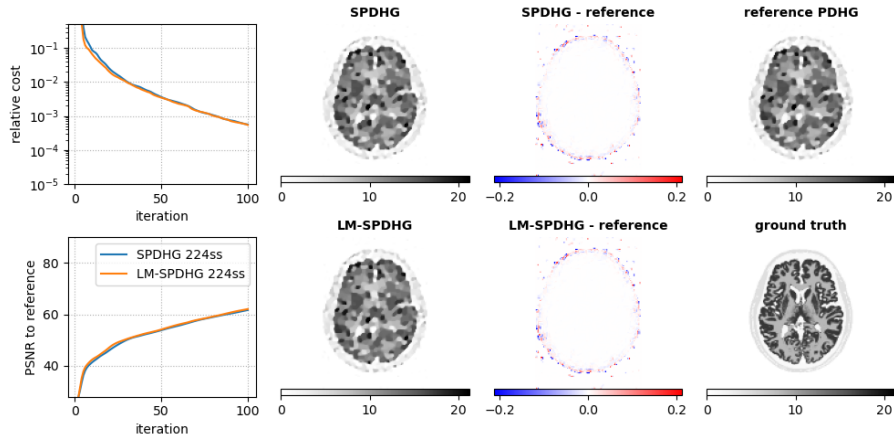
Figure 5 shows the convergence of LM-SPDHG as a function of the number of data subsets used for low ($3e5$) and high ($3e6$) counts and the TV and DTV prior. In general, using 224 subsets leads to faster convergence compared to 56 and 112 subsets. However, for the TV prior, especially at low counts, there is almost no difference between using 56, 112, and 224 subsets. In contrast, for the DTV prior, the difference between using 56, 112, and 224 subsets is more pronounced. For a fixed number of subsets, convergence is faster for high count compared to low count data sets.

Reconstruction of 3D XCAT data

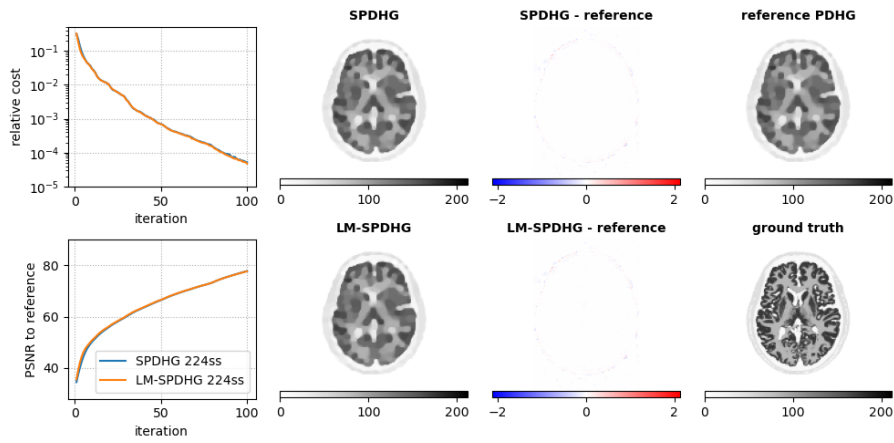
Figure 6 shows the results of the reconstruction of the listmode data simulated from the 3D XCAT phantom using a TV prior with $\beta = 0.03$. From the plot of the cost function and the reconstructions shown in the middle, we can see that reasonable convergence is reached after approximately 25 iterations with 224 subsets. Note that in contrast to our 2D experiments, the cost function initially increases until the 3rd iteration before it decreases and stabilizes after around 25 iterations. As mentioned above, calculating the projections in listmode for $7e7$ counts is roughly a factor of 3 faster compared to sinogram-based processing which substantially speeds up every iteration. Note that in our proof-of-concept implementation, the effective speed up is less than a factor of 3 since we did not implement the gradient operators and proximal mappings on a GPU yet which leads to overhead due to gradient-based updates. However, we expect that, once properly implemented on GPUs, this overhead will be small compared to the time needed to calculate the actual TOF projections.

Reconstruction of NEMQ IQ phantom data

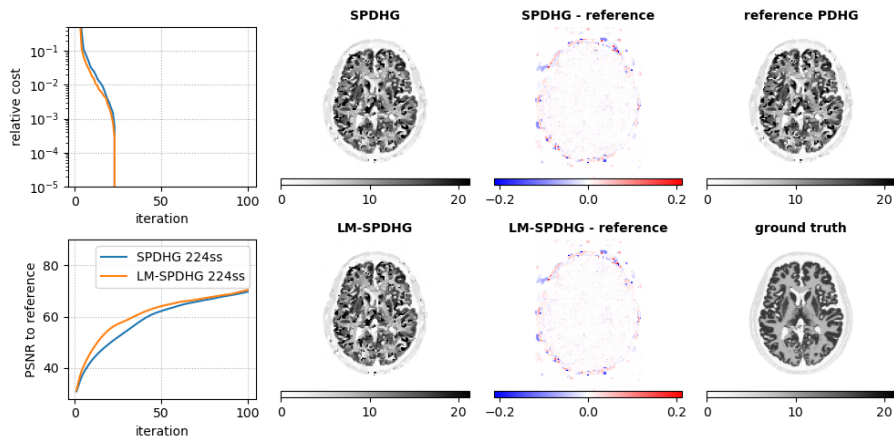
Figure 7 shows the results of the reconstructions of the listmode data from the acquisition of the NEMA image quality phantom on the GE Discovery MI 4 ring TOF PET system. After 100 iterations, LM-SPDHG using 224 subsets has lower cost compared to both EM-TV reconstructions and is closest to the reference reconstruction in terms of PSNR. From the difference images it can be seen that the stochastic LM-SDPHG mostly differs from the reference in the background outside the phantom. In contrast, both EM-TV



(a) 3e5 true (5e5 prompt) counts, TV prior, $\beta = 0.03$

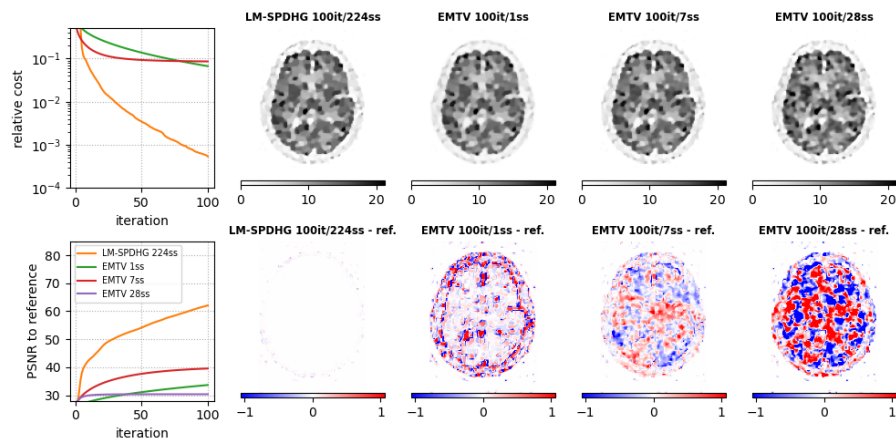


(b) 3e6 true (5e6 prompt) counts, TV prior, $\beta = 0.03$

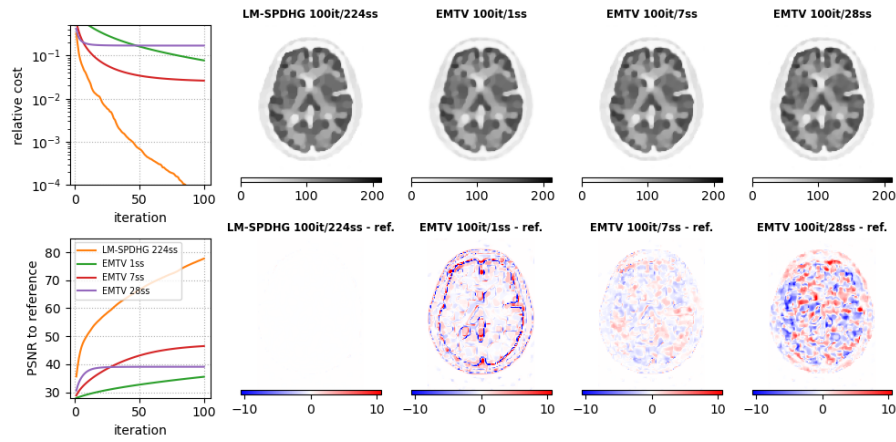


(c) 3e5 true (5e5 prompt) counts, DTV prior, $\beta = 0.1$

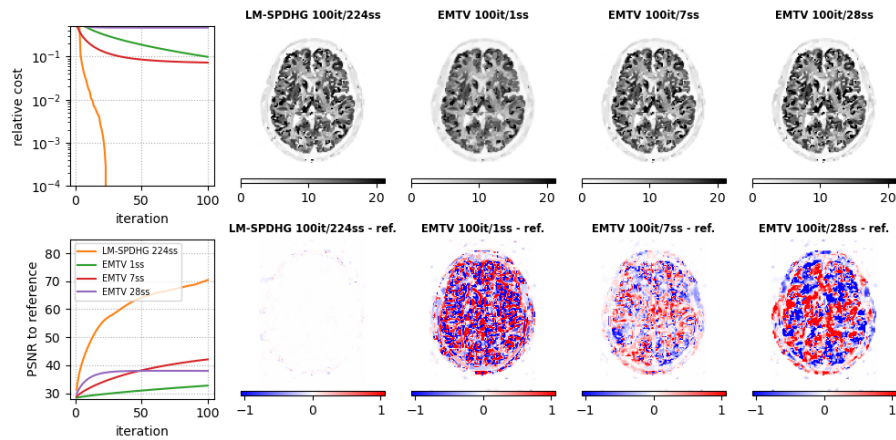
Figure 3: Comparison of convergence of sinogram SPDHG and LM-SPDHG for using 244 subsets. All three subfigures (a) - (c) show the same quantities but for different count levels and priors. Left column: relative cost and PSNR to with respect to the reference solution as a function of the iterations for sinogram SPDHG (blue) and LM-SPDHG (orange). Second column: SPDHG (top) and LM-SPDHG (bottom) reconstruction after 100 iterations. Third column: absolute difference between SPDHG/LM-SPDHG and reference PDHG reconstruction. Forth column: reference PDHG reconstruction using 20000 iterations (top) and ground truth used to generate the data (bottom).



(a) $3e5$ true ($5e5$ prompt) counts, TV prior, $\beta = 0.03$

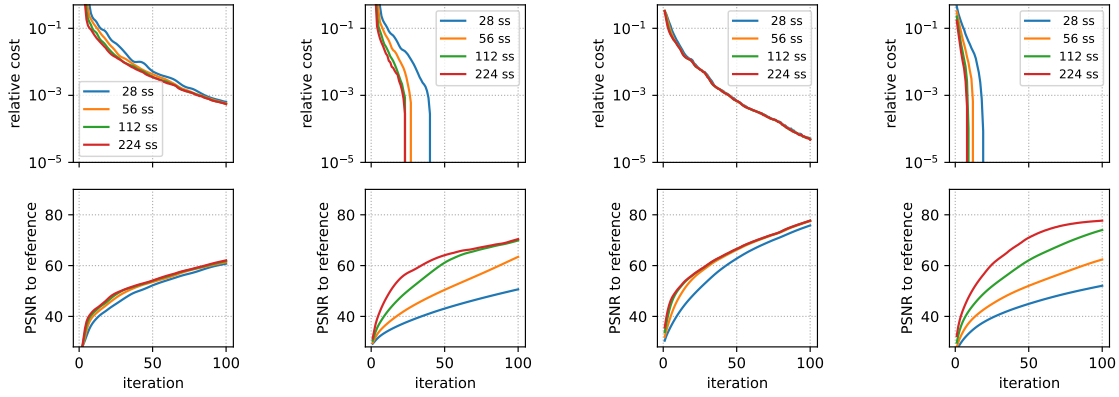


(b) $3e6$ true ($5e6$ prompt) counts, TV prior, $\beta = 0.03$



(c) $3e5$ true ($5e5$ prompt) counts, DTV prior, $\beta = 0.1$

Figure 4: Same as Fig. 3 but comparing the convergence of LM-SPDHG using 224 subsets and listmode EM-TV using 1, 7 and 28 subsets. The top row of images shows the reconstruction after 100 iterations and the bottom row shows the difference to the reference reconstruction which is shown in Fig. 3. Note that the width of the color window in the difference plots is five times wider compared to Fig. 3.



(a) $3e5$ true ($5e5$ prompt) counts, TV prior, $\beta = 0.03$ (b) $3e5$ true ($5e5$ prompt) counts, DTV prior, $\beta = 0.1$ (c) $3e6$ true ($5e5$ prompt) counts, TV prior, $\beta = 0.03$ (d) $3e6$ true ($5e5$ prompt) counts, DTV prior, $\beta = 0.1$

Figure 5: Converge of LM-SPDHG for different number of subsets at two count levels for the TV and DTV prior. Note that when increasing the number of data subsets, the number of gradient updates per iteration increases as well.

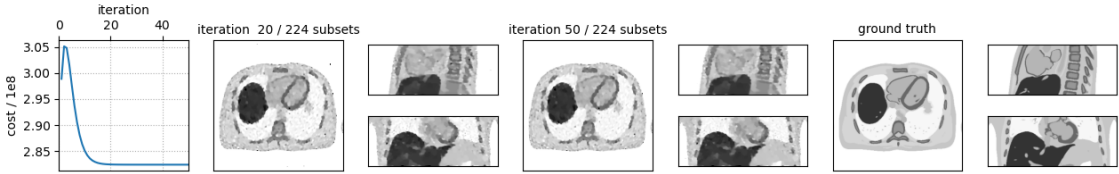


Figure 6: Convergence of LM-SPDHG for reconstruction of 3D TOF data generated from the XCAT phantom using $4e7$ true ($7e7$) prompt counts and a TV prior with $\beta = 0.03$. Left column: evolution of cost function. Columns 2-3: transversal, sagittal and coronal slice of LM-SPDHG reconstruction after 20 iterations and 224 subsets. Columns 4-5: LM-SPDHG reconstruction after 100 iterations and 224 subsets. Columns 6-7: Ground truth image.

reconstructions show bigger residual differences within the phantom which are most pronounced in the “warm” background for EM-TV using 28 subsets and in the “cold” central insert for EM-TV using 1 subset.

4 Discussion

The results of our numerical experiments presented in this work demonstrate that the speed of convergence of LM-SPDHG is essentially the same as the one of the original SPDHG using sinograms. For clinical acquisitions with state-of-the-art TOF PET scanners resulting in extremely sparse data, LM-SPDHG has two distinct advantages compared to SPDHG. First, during the iterations all forward and back projections can be performed in listmode which is faster compared to sinogram projectors for sparse TOF data.

Second, as shown in Table 1, the memory requirements are substantially reduced such that even for an acquisition with $5e8$ prompt coincidences only 12.5 GB of memory are needed. This actually enables a pure GPU-implementation of LM-SPDHG avoiding intermediate memory transfer between the host and a state-of-the-art GPU with a memory of approximately 16 GB. Note that in our proof of concept implementation of LM-SPDHG we used a hybrid computing approach where only the TOF PET forward and back projections were computed using a GPU. We expect that once properly implemented purely on a GPU, the computation time required for LM-SPDHG will further decrease since memory transfer between host and GPU is a bottleneck in our implementation. Note that a pure GPU implementation of the conventional SPDHG algorithm for modern TOF PET data is more complicated since more than 50 GB of GPU is required.

In this proof of concept work, we only used two non-smooth TV-like priors to benchmark LM-SPDHG. Note that in general, SPDHG and LM-SPDHG can be also used for smooth priors as long as the proximal operator of the convex dual of the priors can be efficiently calculated which is e.g. the case for prior

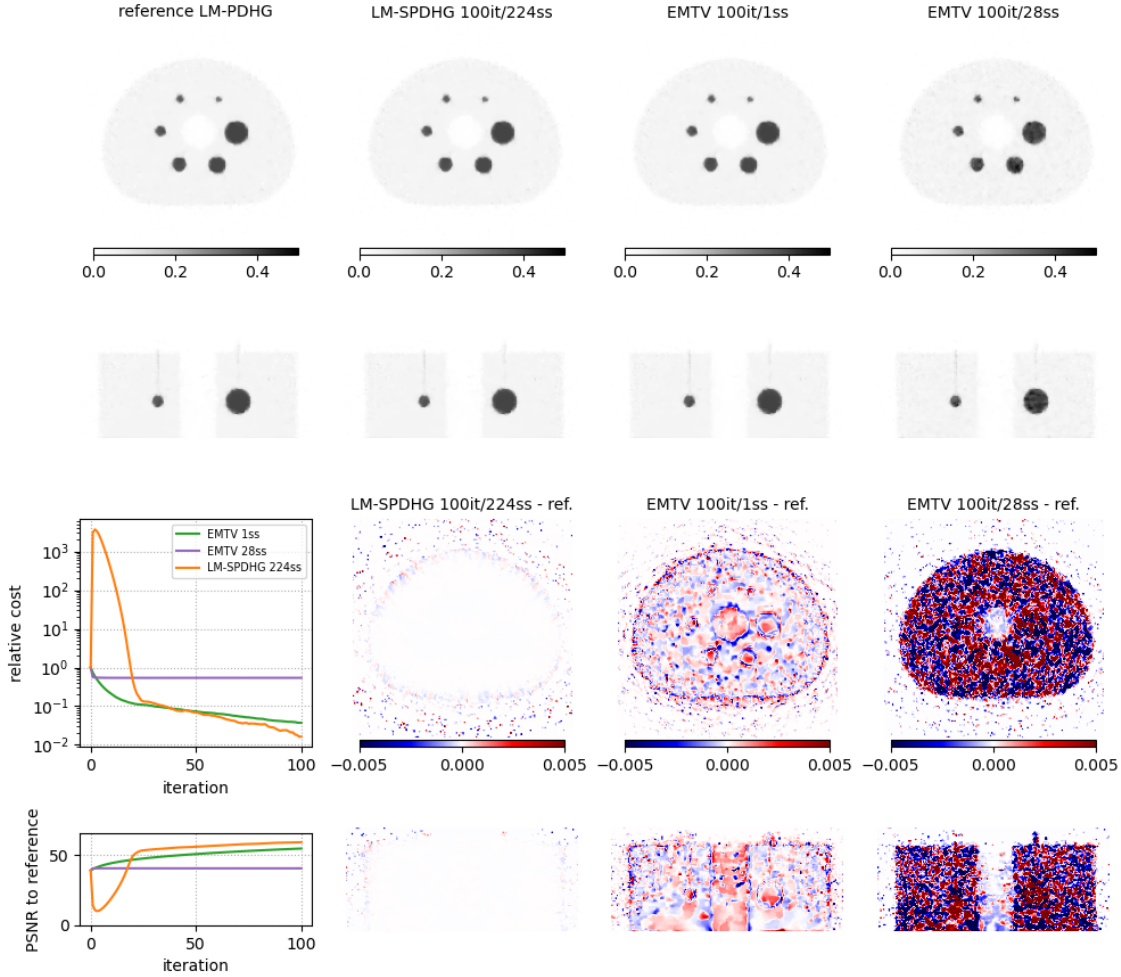


Figure 7: Convergence of LM-SPDHG for reconstruction of real 3D TOF data from an acquisition of the NEMA image quality phantom on a GE Discovery MI 4 ring TOF PET system with a TV prior and $\beta = 6$ with $2.2e7$ true ($4.7e7$ prompt) counts. First column, top two rows: transaxial and coronal slice of reference LM-PDHG reconstruction using 20000 iterations and 1 subset. Second column, top two rows: LM-SPDHG reconstruction using 100 iterations and 224 subsets. Third column, top two rows: EM-TV reconstruction using 100 iterations and 1 subset. Fourth column, top two rows: EM-TV reconstruction using 100 iterations and 28 subsets. First column, bottom two rows: relative cost and PSNR to reference reconstruction. Second, third, fourth column, bottom two rows: absolute difference compared to reference reconstruction.

penalizing the squared L2 norm or Huber TV. However, for smooth priors the speed of convergence of (LM)-SPDHG should be benchmarked against other stochastic gradient-based optimization techniques such as the stochastic variance reduced gradient (SVRG) [19] or SAGA [20] which is beyond the scope of this work. We also note that in this work we used a scalar spatially-invariant prior strength β which leads to a spatially-variant local perturbation response (LPR). For practical applications where a spatially-invariant response is desirable, a spatially-variant prior strength should be used as described in [21, 22]. We emphasize that the listmode EM-TV algorithm is still a very practical and useful algorithm to approximate the solution of the optimization problem (1) for listmode data and non-smooth priors. However, as shown in Fig. 4, it seems that when using ordered subsets for acceleration, EM-TV does not reach the optimal solution but rather remains on a limit cycle similar to the behaviour of OSEM. Whether the difference between the limit cycle and the true optimal solution is of importance for a given count level and clinical task, should be investigated in the future.

As shown in Fig. 5, choosing the “optimal” number of subsets for LM-SPDHG seems to depend on the prior and the number of acquired counts. For a reconstruction of a high-count scan with DT, it is possible

that LM-SPDHG with more than 224 subsets converges even faster. A detailed investigation of the choice of the number of subsets for different acquisition and reconstruction scenarios is left for future research. Last but not least, we would like to note that according to our experience, SPDHG and LM-SPDHG for TOF PET reconstruction also converge for ρ slightly greater than one which might be of interest for practical applications where stopping as early as possible can be important. Suppl. Fig. 3 shows that in our 3D XCAT example, convergence can be further accelerated by using $\rho = 8$ and $\gamma = 30/\|x^0\|_\infty$. A detailed investigation of the convergence speed as a function of ρ and γ potentially involving an iteration-dependent choice of ρ [23] is, however, beyond the scope of this manuscript and left for future research.

5 Conclusion

For sparse TOF data, the proposed LM-SPDHG algorithm severely reduces the memory requirements and computation times compared to the original SPDHG enabling the application of LM-SPDHG in routine clinical practice where short reconstruction times are crucial.

Acknowledgements

The authors would like to thank Claire Delplancke for the insightful discussion on the initialization of (S)PDHG. Moreover, the authors would like to thank Prof. Kristof Baete for the acquisition of the NEMA data set and Dr. Ahmadreza Rezaei for preprocessing of the same data set. This work was supported in part by the NIH grant 1P41EB017183-01A1.

Appendix A Listmode re-formulation of the sinogram-based minimization problem

Here, as basis for the proposed LM-SPDHG algorithm, we provide details on the listmode re-formulation of the sinogram-based minimization problem (1). To this aim, we denote the dependence of $D_i(\cdot)$ on the data d_i explicitly via $D(\cdot; d_i)$. Further, recall that for N the list of detected events, i_e is the sinogram bin in which event $e \in N$ was detected. With $e_0 \notin N$ denoting an additional, artificial event summarizing zero measurements we then obtain

$$\begin{aligned}
\sum_{i=1}^m D((Px + s)_i; d_i) &= \sum_{i=1}^m \sum_{e \in N: i_e=i} \frac{(Px + s)_{i_e}}{d_{i_e}} - \log((Px + s)_{i_e}) + \sum_{i: d_i=0} (Px)_i \\
&= \sum_{e \in N} \frac{(Px + s)_{i_e}}{d_{i_e}} - \log\left(\frac{(Px + s)_{i_e}}{d_{i_e}}\right) - \sum_{e \in N} \log(d_{i_e}) + \sum_{i: d_i=0} (Px)_i \\
&= \sum_{e \in N \cup \{e_0\}} D\left(\frac{(P_N^{LM} x + s^{LM})_e}{d_{i_e}}; d_e^{LM}\right) - \sum_{e \in N} \log(d_{i_e}) \\
&= \sum_{e \in N \cup \{e_0\}} D\left(\hat{P}_N^{LM} x + \hat{s}^{LM}\right)_e; d_e^{LM} - \sum_{e \in N} \log(d_{i_e})
\end{aligned}$$

where $d_e^{LM} = 1$ for $e \in N$, $d_{e_0}^{LM} = 0$, s^{LM} with $s_e^{LM} = s_{i_e}$ is the list-mode random and scatter estimate and

$$(P^{LM} u)_e = \begin{cases} (Pu)_{i_e} & \text{if } e \in N \\ \sum_{i: d_i=0} (Pu)_i & \text{if } e = e_0. \end{cases}$$

The last step uses the rescaled operator \hat{P}^{LM} and the rescaled estimate \hat{s}^{LM} defined as $(\hat{P}^{LM} u)_e = (P^{LM} u)_e / d_{i_e}$ and $(\hat{s}^{LM})_e = s^{LM} / d_{i_e}$ for $e \in N$, and $(\hat{P}^{LM} u)_{e_0} = (P^{LM} u)_{e_0}$ and $(\hat{s}^{LM})_{e_0} = 0$, respectively.

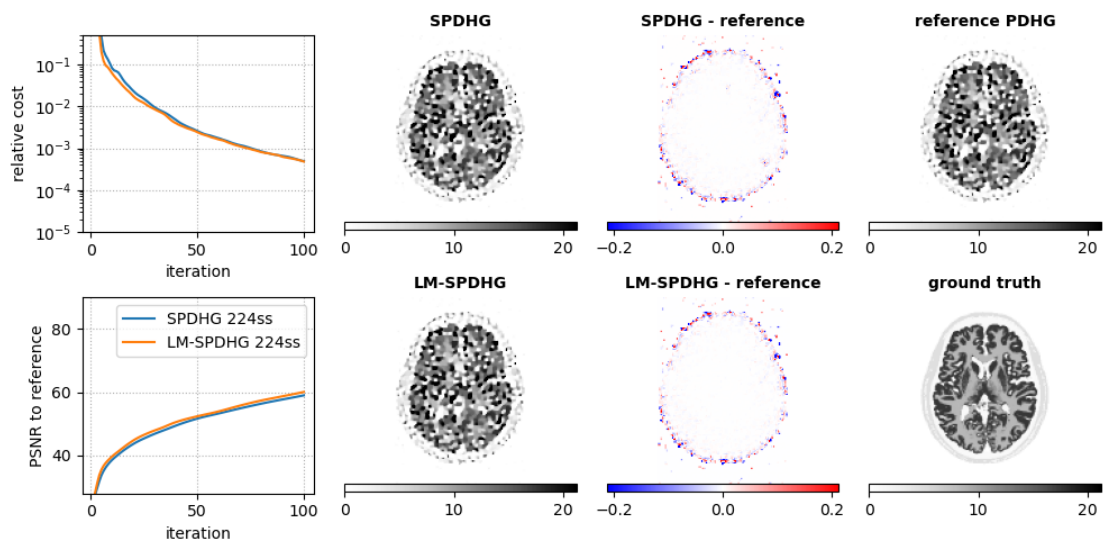
Now the last line of the above reformulation provides an equivalent data term which (after removing the constant $\sum_{e \in N} \log(d_{i_e})$) can be used to obtain an equivalent list-mode-based reformulation of (1).

Applying the SPDHG for this reformulation results in the proposed LM-SPDHG Algorithm 2. Note that there, the non-rescaled operator P^{LM} and estimate s^{LM} appear since i) on line 11 of the algorithm, the rescaling of P^{LM} and s^{LM} cancels out with the rescaling of P^{LM} in the step size S_k of (9), and ii) the rescaling of P^{LM} in line 12 is incorporated explicitly. Furthermore, note that we use the full forward operator P instead of $P_{N_k}^{LM}$ for the stepsize T_k , for reasons explained in the paragraph above the respective equation (9).

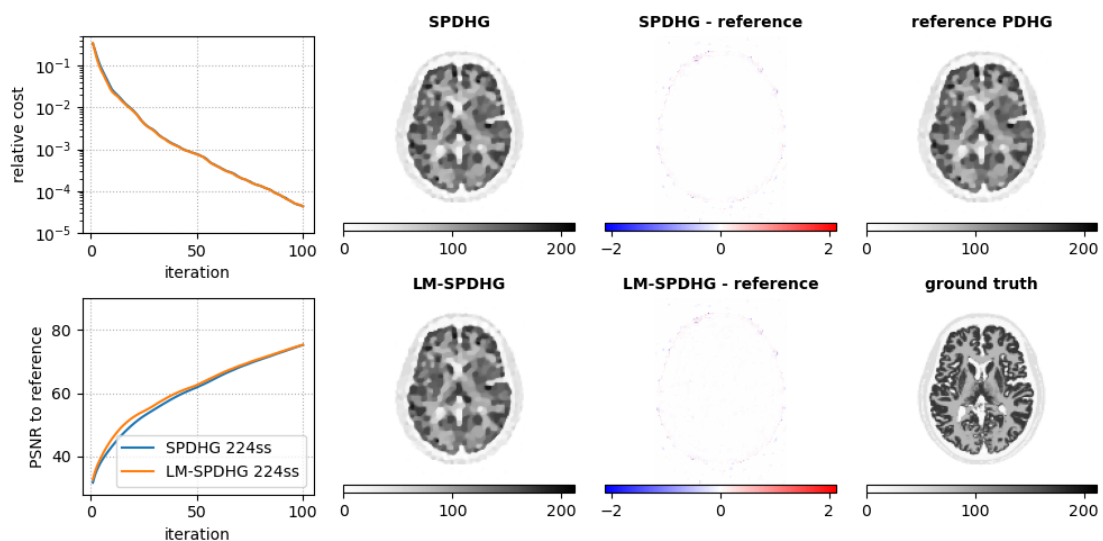
References

- [1] L. I. Rudin, S. Osher, and E. Fatemi. “Nonlinear total variation based noise removal algorithms”. In: *Physica D* 60.1-4 (1992), pp. 259–268.
- [2] K. Bredies, K. Kunisch, and T. Pock. “Total generalized variation”. In: *SIAM Journal on Imaging Sciences* 3.3 (2010), pp. 492–526. DOI: [10.1137/090769521](https://doi.org/10.1137/090769521).
- [3] D. S. Rigie and P. J. La Rivière. “Joint reconstruction of multi-channel, spectral CT data via constrained total nuclear variation minimization.” In: *Physics in medicine and biology* 60.5 (2015), pp. 1741–62. DOI: [10.1088/0031-9155/60/5/1741](https://doi.org/10.1088/0031-9155/60/5/1741).
- [4] F. Knoll, M. Holler, T. Koesters, et al. “Joint MR-PET reconstruction using a multi-channel image regularizer”. In: *IEEE Transactions on Medical Imaging* 36.1 (2016), pp. 1–16. DOI: [10.1109/TMI.2016.2564989](https://doi.org/10.1109/TMI.2016.2564989).
- [5] M. Ehrhardt, P. Markiewicz, M. Liljeroth, et al. “PET Reconstruction with an Anatomical MRI Prior using Parallel Level Sets”. In: *IEEE Transactions on Medical Imaging* 35.9 (2016), pp. 2189–2199. DOI: [10.1109/TMI.2016.2549601](https://doi.org/10.1109/TMI.2016.2549601).
- [6] G. Schramm, M. Holler, A. Rezaei, et al. “Evaluation of Parallel Level Sets and Bowsher’s Method as Segmentation-Free Anatomical Priors for Time-of-Flight PET Reconstruction”. In: *IEEE Transactions on Medical Imaging* 37.2 (2017), pp. 590–603. DOI: [10.1109/TMI.2017.2767940](https://doi.org/10.1109/TMI.2017.2767940).
- [7] M. J. Ehrhardt and M. M. Betcke. “Multicontrast MRI Reconstruction with Structure-Guided Total Variation”. In: *SIAM Journal on Imaging Sciences* 9.3 (2016), pp. 1084–1106.
- [8] A. Chambolle and T. Pock. “A first-order primal-dual algorithm for convex problems with applications to imaging”. In: *Journal of Mathematical Imaging and Vision* 40.1 (2011), pp. 120–145. DOI: [10.1007/s10851-010-0251-1](https://doi.org/10.1007/s10851-010-0251-1).
- [9] A. Chambolle, M. J. Ehrhardt, P. Richtarik, et al. “Stochastic primal-dual hybrid gradient algorithm with arbitrary sampling and imaging applications”. In: *SIAM Journal on Optimization* 28.4 (2018), pp. 2783–2808. DOI: [10.1137/17M1134834](https://doi.org/10.1137/17M1134834).
- [10] M. J. Ehrhardt, P. Markiewicz, and C. B. Schönlieb. “Faster PET reconstruction with non-smooth priors by randomization and preconditioning”. In: *Physics in Medicine and Biology* 64.22 (2019). DOI: [10.1088/1361-6560/ab3d07](https://doi.org/10.1088/1361-6560/ab3d07).
- [11] T. Tomitani. “Image reconstruction and noise evaluation in photon time-of-flight assisted positron emission tomography”. In: *IEEE Transactions on Nuclear Science* 28 (1981), pp. 4581–4589.
- [12] G. Schramm and M. Holler. “Fast and memory-efficient reconstruction of sparse TOF PET data with non-smooth priors”. In: *Proceedings of the 16th Virtual International Meeting on Fully 3D Image Reconstruction in Radiology and Nuclear Medicine*. arXiv, 2021.
- [13] A. Sawatzky, C. Brune, F. Wübbeling, et al. “Accurate EM-TV Algorithm in PET with Low SNR”. In: *IEEE Nuclear Science Symposium Conference Record*. 2008, pp. 5133–5137. DOI: [10.1109/NSSMIC.2008.4774392](https://doi.org/10.1109/NSSMIC.2008.4774392).
- [14] A. Sawatzky, C. Brune, T. Kösters, et al. “EM-TV Methods for Inverse Problems with Poisson Noise”. In: *Level Set and PDE Based Reconstruction Methods in Imaging*. Springer, 2013, p. 110. DOI: [10.1007/978-3-319-01712-9](https://doi.org/10.1007/978-3-319-01712-9).
- [15] P. M. Joseph. “An Improved Algorithm for Reprojecting Rays Through Pixel Images”. In: *IEEE Transactions on Medical Imaging* 1.3 (1982), pp. 192–196. DOI: [10.1109/TMI.1982.4307572](https://doi.org/10.1109/TMI.1982.4307572).
- [16] D. Collins, A. Zijdenbos, V. Kollokian, et al. “Design and construction of a realistic digital brain phantom”. In: *IEEE Transactions on Medical Imaging* 17.3 (1998), pp. 463–468. DOI: [10.1109/42.712135](https://doi.org/10.1109/42.712135).
- [17] W. P. Segars, G. Sturgeon, S. Mendonca, et al. “4D XCAT phantom for multimodality imaging research”. In: *Medical Physics* 37.9 (2010), pp. 4902–4915. DOI: [10.1118/1.3480985](https://doi.org/10.1118/1.3480985).

- [18] D. F. Hsu, E. Ilan, W. T. Peterson, et al. “Studies of a next-generation silicon-photomultiplier-based time-of-flight PET/CT system”. In: *Journal of Nuclear Medicine* 58.9 (2017), pp. 1511–1518. DOI: [10.2967/jnumed.117.189514](https://doi.org/10.2967/jnumed.117.189514).
- [19] R. Johnson and T. Zhang. “Accelerating Stochastic Gradient Descent using Predictive Variance Reduction”. In: *Advances in Neural Information Processing Systems*. Ed. by C. J. C. Burges, L. Bottou, M. Welling, et al. Vol. 26. Curran Associates, Inc., 2013.
- [20] A. Defazio, F. Bach, and S. Lacoste-Julien. “SAGA: A Fast Incremental Gradient Method With Support for Non-Strongly Convex Composite Objectives”. In: *Advances in Neural Information Processing Systems*. Ed. by Z. Ghahramani, M. Welling, C. Cortes, et al. Vol. 27. Curran Associates, Inc., 2014.
- [21] S. Ahn and R. M. Leahy. “Analysis of resolution and noise properties of nonquadratically regularized image reconstruction methods for PET”. In: *IEEE Transactions on Medical Imaging* 27.3 (2008), pp. 413–424. DOI: [10.1109/TMI.2007.911549](https://doi.org/10.1109/TMI.2007.911549).
- [22] Y.-j. Tsai, S. Member, G. Schramm, et al. “Benefits of Using a Spatially-Variant Penalty Strength With Anatomical Priors in PET Reconstruction”. In: *IEEE Transactions on Medical Imaging* 39.1 (2020), pp. 11–22. DOI: [10.1109/TMI.2019.2913889](https://doi.org/10.1109/TMI.2019.2913889).
- [23] T. Goldstein, M. Li, and X. Yuan. “Adaptive primal-dual splitting methods for statistical learning and image processing”. In: *Advances in Neural Information Processing Systems*. 2015, pp. 2089–2097.

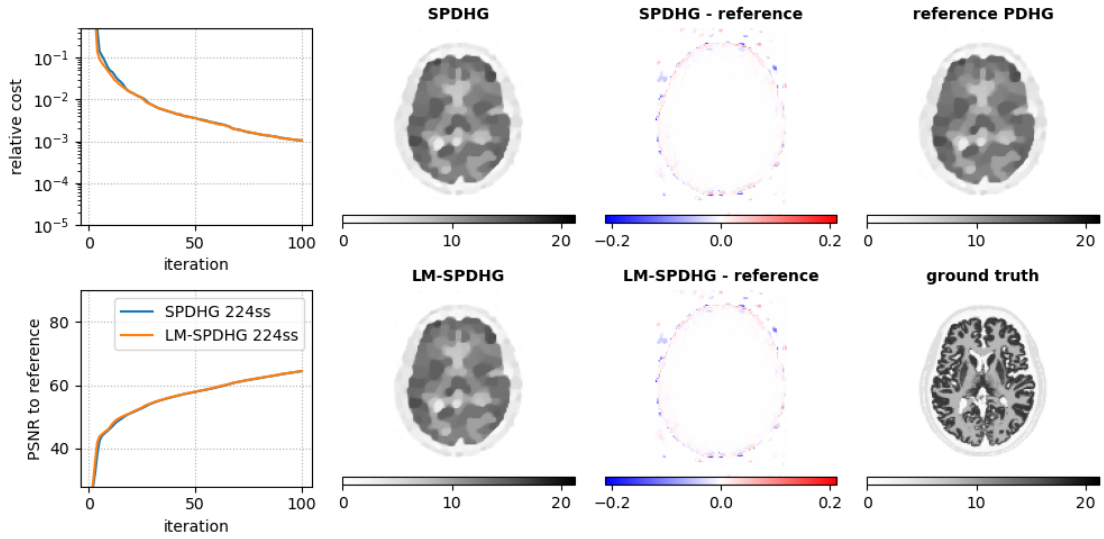


(a) 3e5 true (5e5 prompt) counts, TV prior, $\beta = 0.01$

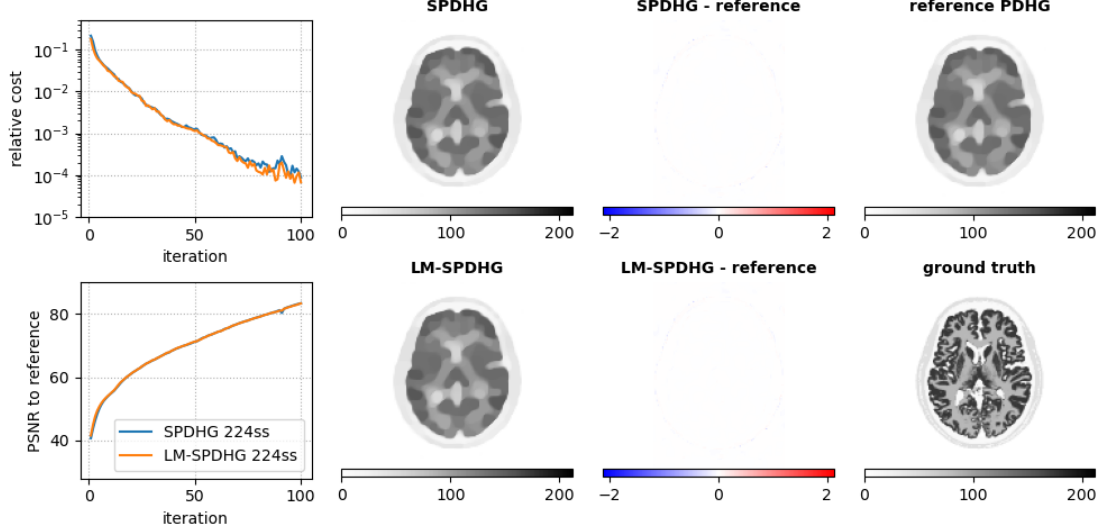


(b) 3e6 true (5e6 prompt) counts, TV prior, $\beta = 0.01$

Supplementary Figure 1: Same as Fig. 3 for a weaker TV prior for low (top) and high counts (bottom).

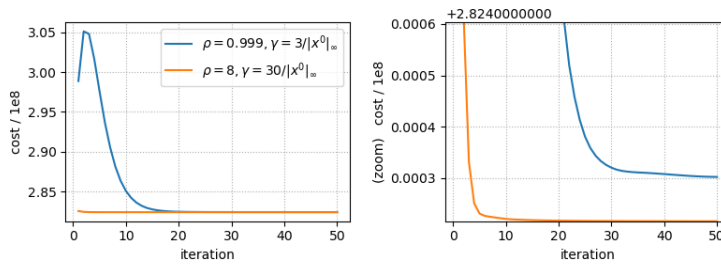


(a) 3e5 true (5e5 prompt) counts, TV prior, $\beta = 0.1$

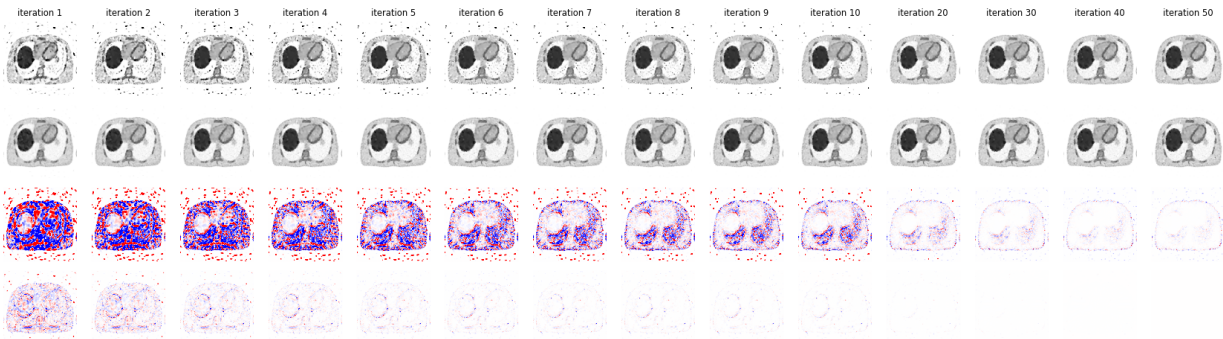


(b) 3e6 true (5e6 prompt) counts, TV prior, $\beta = 0.1$

Supplementary Figure 2: Same as Fig. 3 for a stronger TV prior for low (top) and high counts (bottom).



(a) Evolution of the cost function for two choices of ρ and γ for the 3D XCAT data set.



(b) row 1/2: intermediate reconstructions at different iteration numbers for $\rho = 0.999$, $\gamma = 3/\|x^0\|_\infty$ (row 1) and $\rho = 8$, $\gamma = 30/\|x^0\|_\infty$ (row 2). row 3/4: absolute difference compared to the reconstruction at iteration 50 using $(\rho = 8, \gamma = 30/\|x^0\|_\infty)$. The minimum / maximum of the red-white-blue colormap is -5% / $+5\%$ of the maximum of the reconstruction at iteration 50.

Supplementary Figure 3: Same as Fig. 6 but including a comparison with LM-SPDHG using $\rho = 8$ and $\gamma = 30/\|x^0\|_\infty$. The latter substantially increases the speed of convergence. Note that increasing γ and keeping $\rho = 0.999$ did not increase the speed of convergence.